chemosensors

Article

Electrochemical Detection of Acetaminophen in Pharmaceuticals Using Rod-Shaped α-Bi_2O_3 Prepared via Reverse Co-Precipitation

Ljubica Andjelković [1], Slađana Đurđić [2], Dalibor Stanković [2], Aleksandar Kremenović [3], Vladimir B. Pavlović [4], Dejan A. Jeremić [5] and Marija Šuljagić [1,*]

[1] Institute of Chemistry, Technology and Metallurgy, Department of Chemistry, University of Belgrade, Njegoševa 12, 11000 Belgrade, Serbia; ljubica@chem.bg.ac.rs
[2] Faculty of Chemistry, University of Belgrade, Studentski Trg 12–16, 11000 Belgrade, Serbia; sladjanadj@chem.bg.ac.rs (S.Đ.); dalibors@chem.bg.ac.rs (D.S.)
[3] Faculty of Mining and Geology, University of Belgrade, Djušina 7, 11000 Belgrade, Serbia; aleksandar.kremenovic@rgf.bg.ac.rs
[4] Faculty of Agriculture, University of Belgrade, Nemanjina 6, 11000 Belgrade, Serbia; vladimirboskopavlovic@gmail.com
[5] Innovation Center of the Faculty of Chemistry, University of Belgrade, Studentski Trg 12–16, 11000 Belgrade, Serbia; djeremic@chem.bg.ac.rs
* Correspondence: marija.suljagic@ihtm.bg.ac.rs

Abstract: This study employed a novel synthetic approach involving a modified reverse co-precipitation method utilizing glacial acetic acid to synthesize α-Bi_2O_3. X-ray powder diffraction and scanning and transmission electron microscopy analyses revealed the formation of a rod-like α-Bi_2O_3 microstructure. The prepared material was utilized to modify a glassy carbon paste (GCP) electrode for the development of an electrochemical sensor for acetaminophen (APAP) detection using differential pulse voltammetry (DPV). Cyclic voltammetry studies revealed that the GCP@Bi_2O_3 electrode exhibited enhanced electrochemical properties compared to the bare GCP. The designed GCP@Bi_2O_3 sensor detected APAP in the linear concentration range from 0.05 to 12.00 μM, with LOQ and LOD of 36 nM and 10 nM, respectively. Additionally, the developed sensor demonstrated sufficient precision, repeatability, and selectivity toward APAP detection. The recovery values between the declared and found APAP content in a pharmaceutical formulation (Caffetin®) displayed the advantageous accuracy, precision, and applicability of the GCP@Bi_2O_3 sensor and the developed DPV method for real-time APAP detection in pharmaceuticals, with minimal interference from the matrix effect.

Keywords: rod-like α-Bi_2O_3 microstructure; reverse co-precipitation synthesis; electrochemical sensor; acetaminophen detection

check for updates

Citation: Andjelković, L.; Đurđić, S.; Stanković, D.; Kremenović, A.; Pavlović, V.B.; Jeremić, D.A.; Šuljagić, M. Electrochemical Detection of Acetaminophen in Pharmaceuticals Using Rod-Shaped α-Bi_2O_3 Prepared via Reverse Co-Precipitation. *Chemosensors* **2024**, *12*, 122. https://doi.org/10.3390/chemosensors12070122

Academic Editor: Jagotamoy Das

Received: 7 June 2024
Revised: 27 June 2024
Accepted: 28 June 2024
Published: 2 July 2024

1. Introduction

Acetaminophen, also known as N-acetyl-p-aminophenol (APAP), is a popular and extensively used over-the-counter analgesic and antipyretic drug. It is commonly employed to alleviate mild to moderate pain, fever, and discomfort associated with various conditions, including headaches, muscle aches, menstrual cramps, and cold or influenza symptoms. Its therapeutic effect is achieved through the inhibition of prostaglandin synthesis in the central nervous system and sedation of the hypothalamic center responsible for thermoregulation [1]. Acetaminophen is considered safer than non-steroidal anti-inflammatory drugs for individuals with certain medical conditions, as it does not exhibit significant anti-inflammatory or anticoagulant effects [2,3]. Its popularity stems from its effectiveness in managing pain and fever while being well-tolerated at recommended dosages. However, excessive or prolonged use of acetaminophen may lead to potential hepatotoxicity as a consequence of the accumulation of toxic metabolites [4–6].

It is crucial to detect and accurately quantify APAP in pharmaceutical formulations and biological samples for several reasons: dosage monitoring, quality control in pharmaceuticals, toxicology, and forensics, and bioavailability and pharmacokinetic studies to understand its metabolism and properties for drug development and optimization. The pursuit of developing simple, rapid, accurate, and sensitive analytical methods for determining APAP remains a focus within the scientific community [7]. Numerous techniques have been developed thus far, including liquid chromatography [8–11], spectrophotometry [12–14], chemiluminescence [15–17], titrimetry [18,19], electrophoresis [20–22], spectrofluorimetry [23–25], as well as electrochemical techniques [1,12,26–28]. While some approaches, such as spectrophotometry and chemiluminescence, demand tedious sample preparation, others, like liquid chromatography, can be time-consuming. Electroanalytical techniques stand out among the rest due to their rapidity, selectivity, high sensitivity, simplicity, and cost-effectiveness. Additionally, sample preparation is not required. Since acetaminophen exhibits electroactive properties, electrochemical techniques emerge as the preferred choice for its determination.

Bismuth oxide (Bi_2O_3) is a material of significant interest in modern solid-state technology due to its distinctive structures and functional properties, such as a wide energy band gap, high refractive index, high dielectric permittivity, as well as notable photoconductivity and photoluminescence [29,30]. These remarkable features enable the potential application of Bi_2O_3 in various fields, including sensors [31–35], optical coatings [36,37], photovoltaic cells [38], solid oxide fuel cells [39–41], superconductors [42–44], and catalysts [45–51]. The phase composition of a material is a well-known key factor influencing its functional properties. Also, catalytic activity is closely related to crystalline structure, morphology, and particle size. Therefore, the controlled synthesis of specific Bi_2O_3 phases is of great importance. Bismuth oxide crystallizes in six primary polymorphic forms. Monoclinic (α-Bi_2O_3) and cubic face-centered (δ-Bi_2O_3) forms represent low- and high-temperature stable phases, respectively. In contrast, phases denoted as β-Bi_2O_3 (tetragonal structure), γ-Bi_2O_3 (cubic, body-centered structure), ε-Bi_2O_3 (orthorhombic structure), and ω-Bi_2O_3 (triclinic structure) are high-temperature metastable phases [52]. The chosen preparation procedures and synthesis conditions influence the transitions between Bi_2O_3 phases. In recent decades, promising catalytic activity has been exhibited in specific Bi_2O_3 structures (rods, wires, tubes, or fibers), attracting scientific interest in developing new synthetic methods to produce novel Bi_2O_3 structures [52–57]. Numerous physical and chemical procedures have been developed for the preparation of Bi_2O_3, including pulsed laser deposition [58–61], epitaxial growth [62–64], plasma [65,66], magnetron sputtering [67,68], vapor transport method [69,70], co-precipitation [71–74], chemical vapor deposition [75–77], sonochemical [78–81], and hydrothermal [56,82–84]. Chemical preparation methods are the most convenient for large-scale industrial manufacturing. Co-precipitation is a relatively inexpensive and straightforward method. However, the main challenges associated with this procedure are particle size and morphology, which can be highly variable. Nonetheless, these factors can be controlled by carefully selecting synthesis conditions.

In this work, we present the synthesis of α-Bi_2O_3 rod-like microstructures via reverse co-precipitation, which can potentially be used in catalytic applications. Conventional co-precipitation and reverse co-precipitation routes typically involve the use of nitric acid (HNO_3) to dissolve bismuth nitrate ($Bi(NO_3)_3$) as a source of Bi^{3+} ions [72,85,86]. This research describes a modified reverse co-precipitation procedure for synthesizing Bi_2O_3 using glacial acetic acid instead of nitric acid and applying Bi_2O_3 material in the development of an electrochemical sensor. No previous reports exist on preparing Bi_2O_3 rods by reverse co-precipitation using glacial acetic acid. A few structural and morphological characterization techniques confirmed the formation of monoclinic α-Bi_2O_3 rod-like microstructures. The synthesized α-Bi_2O_3 material was utilized to modify the glassy carbon paste to produce an electrochemical sensor. Differential pulse voltammetry (DPV) was used as an electroanalytical method for detecting APAP. Subsequently, the proposed electrochemical platform was successfully applied to determine APAP in pharmaceutical formulation.

2. Materials and Methods

2.1. Chemicals and Solutions

APAP (BioXtra $\geq$ 99.0%), potassium chloride (KCl, 99.9%), potassium hexacyanoferrate(II) trihydrate [$K_4[Fe(CN)_6] \times 3H_2O$, >98.5%), potassium hexacyanoferrate(III) [$K_3[Fe(CN)_6]$, 99%), boric acid (H_3BO_3, 99.97% trace metals basis), phosphoric acid [H_3PO_4, ACS reagent, $\geq$85 wt. % in H_2O), acetic acid [CH_3COOH, glacial, ACS reagent, $\geq$99.7%], sodium hydroxide (NaOH, ACS reagent, $\geq$97.0%), bismuth(III) nitrate pentahydrate ($Bi(NO_3)_3 \times 5H_2O$, ACS reagent, $\geq$98.0%), glassy carbon powder (glassy, spherical powder, 2–12 µm, 99.9% trace metals basis), and mineral oil were supplied by Merck, Darmstadt, Germany.

Merck (Darmstadt, Germany) also delivered chemical compounds used as interfering substances (potassium nitrate (KNO_3, powder, ACS reagent, $\geq$99.0%), sodium sulfate decahydrate ($Na_2SO_4 \times 10H_2O$, powder, ACS reagent, $\geq$99.0%), D-glucose (powder, ACS reagent), and caffeine (powder, ReagentPlus®)).

The Britton–Robinson buffer solution (BRBS) was prepared using a step-by-step process. First, 2.80 mL of H_3PO_4 ($\geq$85 wt. % in H_2O) was dissolved, followed by 2.40 mL of CH_3COOH (glacial, $\geq$99.7%). Then, 2.48 g of H_3BO_3 was added to the mixture. Finally, the entire solution was dissolved in 1000 mL of deionized water.

The APAP standard solution (0.0050 mol/L) was prepared by dissolving a specific amount of APAP powder ($\geq$99.0%) in deionized water.

2.2. Preparation Procedures

2.2.1. Synthesis of Bi_2O_3 Particles

Modified reverse co-precipitation was used to prepare Bi_2O_3 particles [72]. This synthesis starts with the acid-dissolved reactants introduced dropwise into the base solution to form the desired precipitate due to maintaining a high pH value. Glacial acetic acid dissolved $Bi(NO_3)_3 \times 5H_2O$. The final concentration of Bi^{3+} ions was 0.03 M. The obtained solution was added dropwise into the excess NaOH solution (pH $\approx$ 13). The Bi_2O_3 yellow precipitate was formed, and the suspension was heated at 80 °C for 1 h. The pH of the suspension was about 11. Furthermore, the precipitate was filtered, rinsed three times with deionized water, and dried at ambient temperature for 24 h. The powder was pulverized in an agate mortar and annealed in an electrical furnace with a heating rate of 10 °C/min at 450 °C for 1 h.

2.2.2. Preparation of Working Electrodes

Homogeneous bare glassy carbon paste (GCP) was prepared by hand-mixing 20% mineral oil and 80% glassy carbon powder in a mortar for approximately 20 min. The working electrode was prepared by filling a Teflon tube (with an inner diameter of 2 mm) with the prepared paste. After filling the Teflon tube, the electrode was mechanically polished using weight paper to get a smooth and shiny-looking electrode surface. Subsequently, an electrode was used for electrochemical measurements [87].

The GCP modification was performed by hand-mixing 20% mineral oil, different amounts of Bi_2O_3 modifier (1.0, 2.5, and 5.0%), and glassy carbon powder (up to 80%) in a mortar and pestle for approximately 20 min. The working electrode prepared according to this procedure was labeled GCP@Bi_2O_3. The Teflon tube was filled, and the electrode was polished like the bare GCP. All prepared pastes were stored in the fridge at 4 °C [87].

2.2.3. Preparation of Real Samples

Caffetin® pharmaceutical formulation (Alkaloid, Skopje, Macedonia) was used as a real sample in this study. Per the manufacturer's instructions, each tablet contains 250 mg of APAP. The detailed content of Caffetin® tablets is placed in the Supplementary Material (Addition S1. The detailed content of Caffetin® tablets). The content of the target analyte was determined in three tablets taken randomly from the pharmaceutical packaging box. The previously reported procedure was followed to prepare Caffetin® tablets, which were slightly modified [88,89]. Tablets are prepared identically: the whole tablet was crushed in a mortar with a pestle, and the obtained powder was quantitatively transferred to a voltammetric flask of 100 mL, topped up with distilled water, and stirred for 2 h (solution A). Then, 5 mL of solution A was transferred to a 10 mL voltammetric flask and topped with distilled water (solution B). The standard addition method was used to determine APAP content in Caffetin® pharmaceutical formulations.

2.3. Methods

2.3.1. Structural Characterization of Material

A Rigaku SmartLab diffractometer was used for the X-ray powder diffraction experiment (XRPD). The diffractometer was equipped with $CuK_{\alpha 1,2}$ radiation. It used the generator voltage and the generator current of 40 kV and 30 mA, respectively. The recording range between 4 and 90 $2\theta^\circ$ was used in a continuous scan mode with a scanning step size of 0.01 $2\theta^\circ$ and a scan rate of 5 $2\theta^\circ$/min by the D/TeX Ultra high-speed detector. The phase composition of the synthesized material, the unit cell parameters, and the size-strain values for *P2₁/c* polymorph (α-Bi_2O_3) as well as the phase abundances for $P2_1/c$ polymorph (α-Bi_2O_3) and *P31c* polymorph (ω-Bi_2O_3), calculated by the relative intensity ratio (RIR) method, were obtained with the use of the PDXL2-integrated X-ray powder diffraction software (Ver. 2.8.4.0; Rigaku Corporation, Tokyo, Japan).

Fourier-transform infrared spectroscopy (FTIR) was recorded on a Nicolet 6700 FTIR instrument (Thermo Scientific, Waltham, MA, USA) in the range of 4000–400 cm^{-1} using the attenuated total reflectance (ATR) technique with a Smart Orbit accessory (diamond crystal).

To gain deeper insight into the morphology and elemental composition of the prepared material, scanning electron microscopy (SEM) (JEOL JSM-6390 LV, JEOL Ltd., Peabody, MA, USA) coupled to electron-dispersive spectroscopy (EDS) (Oxford Instruments X-MaxN, Concord, MA, USA) was used. The accelerating voltage was between 20 and 30 kV. The transmission electron microscopic (TEM) analysis was performed on a JEOL JEM-1400 Plus Electron microscope (JEOL Ltd., Peabody, MA, USA)with a voltage of 120 kV and a LaB_6 filament at a magnification of 1500×.

2.3.2. Electrochemical Measurements

All experiments were performed using a *PalmSens4* instrument (Houten, Utrecht, The Netherlands) equipped with PSTrace voltammetric software (Version 5.8). This study used a conventional three-electrode cell (25 mL), with unmodified/modified glassy carbon paste as a working electrode, a platinum sheet electrode (Methrom AG, Herisau, Switzerland) as the auxiliary electrode, and silver/silver chloride (3 mol/L KCl, Ag/AgCl, Methrom, Switzerland) as the reference electrode.

3. Results and Discussion

3.1. Structural and Morphological Characterization of Bi_2O_3 Material

The XRPD results confirmed the presence of Bi_2O_3, predominantly composed of $P2_1/c$ polymorph (α-Bi_2O_3) modification (96.3(1)%), as shown in Figure 1A. The obtained unit cell parameters were close to the reference values (PDF # 01-070-8243) (Table S1). The other polymorph modification of ω-Bi_2O_3 (*P31c*) was found in the minority (3.7(1)%), so the calculation of unit cell and microstructural parameters could not be determined with a good confidence level. The presence of Bi_2O_3 ($P2_1/c$, PDF # 01-080-2589) and Bi_6O_7 (*I4/mmm*, PDF # 03-065-5490) near the limit of detection might be possible.

FTIR spectroscopy was used to confirm the identification of the bismuth oxide phases given by the XRPD pattern. Figure 1B shows the FTIR spectrum of the synthesized material. The band at 1389.0 cm^{-1} originates from the vibration of the -NO_3 group, which indicates the existence of nitrate residues attached to the Bi_2O_3 surface [90,91]. The sharp peak at 846.7 cm^{-1} can be attributed to the Bi-O-Bi vibration modes [92,93]. A strong absorption band at 503.7 cm^{-1} is due to the Bi–O stretching mode [51,94].

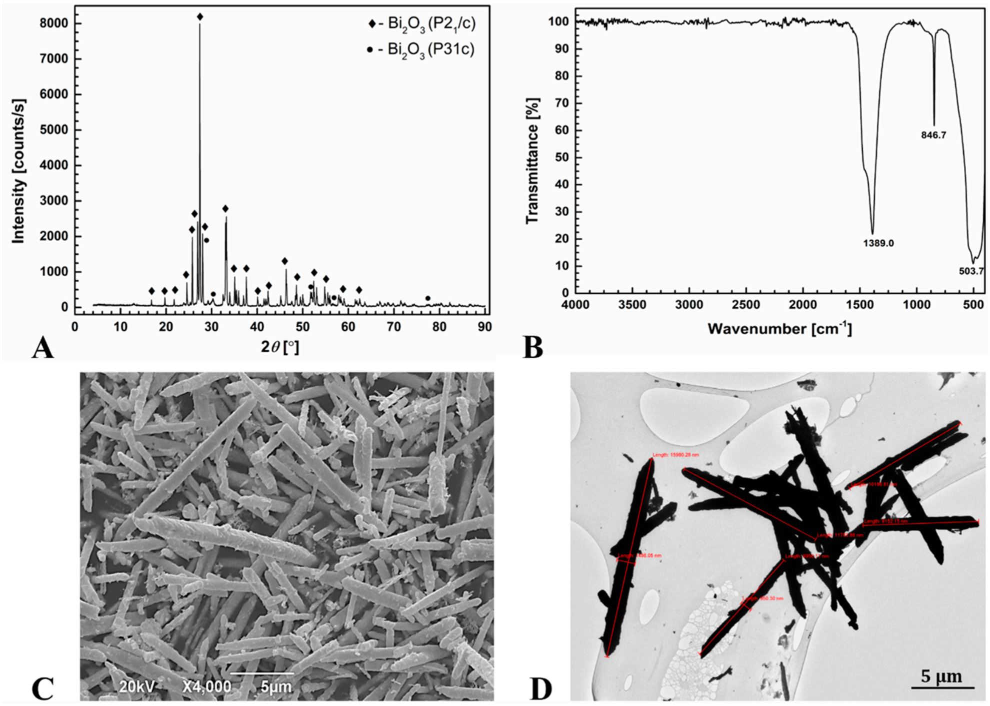

Figure 1. (**A**) X-ray powder pattern of the synthesized Bi_2O_3, (**B**) FTIR spectrum of the synthesized Bi_2O_3, (**C**) SEM, and (**D**) TEM micrographs of the synthesized Bi_2O_3.

The SEM results are presented in Figure 1C. The Bi_2O_3 particles predominantly exhibited a rod-shaped morphology. Other observed morphologies can be attributed to minor phases identified by XRPD analysis. Additionally, this can be attributed to the presence of amorphous, unorganized α-Bi_2O_3 particles. EDS confirmed the high purity level of the obtained sample (Figure S1). Mitsunori et al. also obtained rod-like α-Bi_2O_3 particles in the micrometric range using a co-precipitation route at 80 °C reaction mixture temperature with a nitric acid solution [95]. Notably, they obtained particles with lengths of several tens of micrometers. In the present work, the Bi_2O_3 particles prepared by a modified reverse co-precipitation route combined with calcination are smaller in size.

The TEM micrograph (Figure 1D) confirmed the presence of long rod-shaped particles in the micrometer range. Most particles were approximately 10 μm or longer and had a width of around 1 μm.

3.2. Electrochemical Characterization of Working Electrodes

Cyclic voltammetric and electrochemical impedance spectroscopic analysis. Electrochemical behavior of APAP over a GCP@Bi_2O_3 sensor.

Cyclic voltammetry was used to investigate the electrochemical characteristics of bare GCP and GCP modified with Bi_2O_3 particles (GCP@Bi_2O_3). In this study, GCP was modified with 2.5% Bi_2O_3 particles. Cyclic voltammetric measurements were applied in the potential range of −1.0 V to 1.0 V. Five millimolar $[Fe(CN)_6]^{4-}/[Fe(CN)_6]^{3-}$ in 0.1 M KCl was used as the tested analyte. Figure 2A depicts the cyclic voltammetric response of bare GCP and GCP@Bi_2O_3 in 0.1 M KCl containing 5 mM $[Fe(CN)_6]^{4-}/[Fe(CN)_6]^{3-}$ with a scan rate of 50 mV/s. Both working electrodes allowed well-defined redox peaks in the $[Fe(CN)_6]^{4-}/[Fe(CN)_6]^{3-}$ system. The GCP@Bi_2O_3 electrode showed a higher current intensity of oxidation ($I_{p(ox)}$) and reduction peaks ($I_{p(red)}$) and better reversibility of the redox probe (different between oxidation peak potential ($E_{p(ox)}$) and reduction peak potential ($E_{p(red)}$), ΔE) compared to bare GCP (for GCP@Bi_2O_3: $I_{p(ox)}$ = 29.5 μA, $I_{p(red)}$ = −22.4 μA, ΔE = 0.633 V; for bare GCP: $I_{p(ox)}$ = 24.4 μA, $I_{p(red)}$ = −19.3 μA, ΔE = 0.687 V). A similar trend to cyclic voltammetric measurements was noticed during the EIS analysis. Figure 2B represents Nyquist plots of bare GCP and GCP@Bi_2O_3 electrodes. The obtained Nyquist plots are characterized by a semicircular diameter and a linear part. The charge transfer resistance (*Rct*) at the surface of working electrodes can be determined from the semicircular diameter by extrapolation. The conductivity on the electrode surface can be defined based on the obtained *Rct* values (*Rct* is inversely proportional to conductivity). The linear part of the Nyquist plot refers to the diffusion of $[Fe(CN)_6]^{4-}/[Fe(CN)_6]^{3-}$ analyte [87,96]. Bare GCP was defined with an *Rct* of 37.4 kΩ. On the contrary, the GCP@Bi_2O_3 electrode provided an *Rct* of 26.8 kΩ, indicating a positive influence on the conductivity on the electrode surface after introducing the Bi_2O_3 modifier.

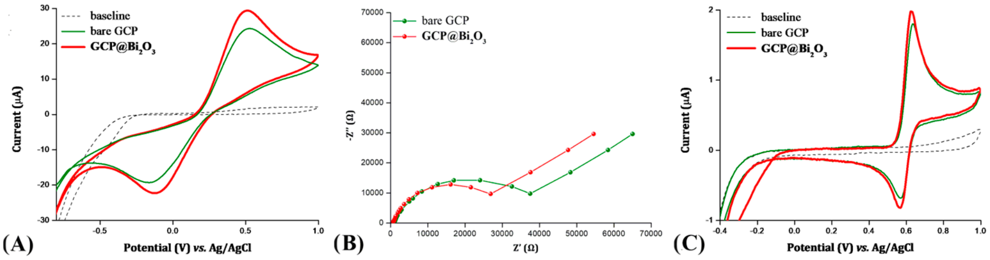

Figure 2. (**A**) Cyclic voltammograms of 5 mM $[Fe(CN)_6]^{4-}/[Fe(CN)_6]^{3-}$ in 0.1 M KCl at bare GCP and GCP@Bi_2O_3 electrode; a scan rate of 50 mV/s. (**B**) EIS spectra in the form of Nyquist plots at bare GCP and GCP@Bi_2O_3 electrodes in 0.1 M KCl containing 5 mM $[Fe(CN)_6]^{4-}/[Fe(CN)_6]^{3-}$. (**C**) Cyclic voltammetric profile of 10 µM APAP in BRBS pH = 3 recorded by bare GCP and GCP@Bi_2O_3 electrode; a scan rate of 50 mV/s.

The electrode surface area (ESA) and heterogeneous rate constant (k^0) of working electrodes were calculated using Equation (1) [87] and Equation (2) [97], respectively, as follows:

$$I_p = 2.69 \times 10^5 \; A \; n^{\frac{3}{2}} \; C \; D^{\frac{1}{2}} \;\; v^{\frac{1}{2}} \tag{1}$$

where I_p—the peak current (A), n—the number of electrons (n = 1), A—the electrode surface area (cm^2), D—the diffusion coefficient (6×10^{-6} cm^2/s for the redox probe), C—the concentration of the redox probe (mol/mL), and ν—the scan rate (V/s).

$$\Delta E = 201.39 log\left(\frac{\nu}{k^0}\right) - 301.78 \tag{2}$$

where ΔE—the difference between $E_{p(ox)}$ and $E_{p(red)}$ (V) and ν—the scan rate (V/s).

The ESA for bare GCP and GCP@Bi_2O_3 were 0.033 cm^2 and 0.040 cm^2, respectively, indicating an increase in the electroactive sites on the electrode surface after GCP was modified with Bi_2O_3 material. The k^0 was calculated at 15.742×10^{-4} 1/s for bare GCP and 15.752×10^{-4} 1/s for GCP@Bi_2O_3 electrode. These results show a higher electron transfer rate at the surface of the GCP@Bi_2O_3 electrode than bare GCP.

Glassy carbon powder is characterized by high conductivity [98], while Bi_2O_3 material is exemplified by catalytic activity and a high surface area [52–57,99]. The synergistic effect of glassy carbon powder and Bi_2O_3 particles can be attributed to an increase in the current intensity of the redox peaks, better reversibility, favorable conductivity at the electrode surface, a higher ESA, and a higher k^0 recorded by the GCP@Bi_2O_3 electrode. By introducing a Bi_2O_3 modifier in carbon paste electrodes, improvements in the electrochemical performances were noticed in several research papers [97,100,101].

Cyclic voltammetry was also used to investigate the electrochemical response of bare GCP and GCP@Bi_2O_3 electrodes toward the main analyte. Figure 2C represents the cyclic voltammetric profile of working electrodes in BRBS pH = 3, containing 10 mM APAP, with a scan rate of 50 mV/s. Both working electrodes provided oxidation and reduction of APAP under both experimental and instrumental conditions. APAP oxidation occurred at around 0.63 V, while the APAP reduction peak was at around −0.57 V. Additionally, more intense APAP redox peaks ($I_{p(ox)}$ = 1.95 µA, $I_{p(red)}$ = −1.28 µA) were recorded with the GCP@Bi_2O_3 electrode compared to bare GCP ($I_{p(ox)}$ = 1.67 µA, $I_{p(red)}$ = −0.99 µA). These results additionally demonstrated improvement in the electrochemical response of the CPE after introducing the Bi_2O_3 material into a glassy carbon paste.

Additionally, the influence of the modifier amount in the GCP on the electrochemical behavior of APAP was examined by cyclic voltammetry. The electrochemical response of the GCP@Bi_2O_3 electrodes (where GCP was modified with 1.0, 2.5, and 5.0% of Bi_2O_3) was followed in BRBS pH = 3 containing 10 μM APAP under a scan rate of 50 mV/s. The GCP with a 2.5% modifier provided the most intense APAP redox peaks. Therefore, GCP modified with 2.5% Bi_2O_3 was used for further experiments.

3.2.1. Effect of pH

The effect of the pH of the BRBS on the electrochemical response of the GCP@Bi_2O_3 sensor towards APAP was investigated using cyclic voltammetry. Figure 3A depicts the cyclic voltammetric profile of 10 μM APAP in BRBS at various pH values (from pH = 2 to pH = 8) over the GCP@Bi_2O_3 electrode (at a scan rate of 50 mV/s). Each pH examined provided the target analyte's oxidation and reduction peak (Figure 3A). Compared to the appearance of the peaks, the favorable shape of the redox peaks of APAP was registered in BRBS pH = 6 (Figure 3A). Therefore, BRBS pH = 6 was selected as the most convenient, and this supporting electrolyte was used in further electrochemical analysis.

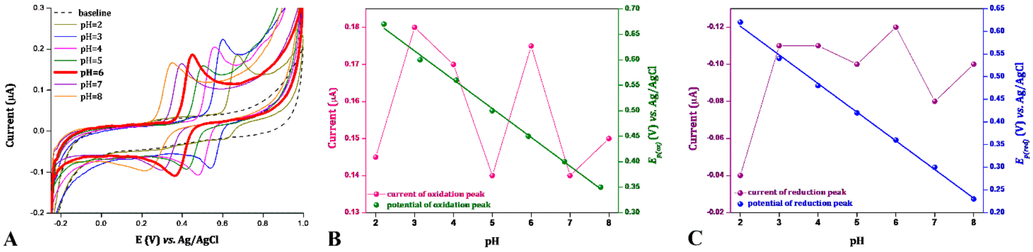

Figure 3. (**A**) Cyclic voltammetric profile of 10 μM APAP in BRBS at different pH values recorded using the GCP@Bi_2O_3 sensor with a scan rate of 50 mV/s. (**B**) Linear plot of oxidation peak current (μA) and $E_{p(ox)}$ vs. pH at the GCP@Bi_2O_3 electrode in the presence of 10 μM APAP. (**C**) Linear plot of reduction peak current (μA) and $E_{p(red)}$ vs. pH at the GCP@Bi_2O_3 electrode in the presence of 10 μM APAP.

In addition, increasing the pH leads to shifts in APAP oxidation and a reduction in peak potentials to negative potential values. In BRBS pH = 2, the oxidation and reduction peaks of the analyte occur at 0.67 V and −0.02 V; at pH = 8, these peaks are shifted to 0.17 V and −0.10 V, respectively (Figure 3A). The plots of $E_{p(ox)}$ vs. pH (Figure 3B) and $E_{p(red)}$ vs. pH (Figure 3C) show high linearity for APAP redox peaks. These linearities can be expressed by Equations (3) and (4):

$$E_{p(ox)}(V) = 0.767 - 0.054\ pH\ (r = -0.999) \tag{3}$$

$$E_{p(red)}(V) = 0.738 - 0.063\ pH\ (r = -0.999) \tag{4}$$

The obtained slopes of −54 mV/pH (for the oxidation peak) and −63 mV/pH (for the reduction peak) indicated an equal number of electrons and protons involved in the oxidation and reduction processes of APAP at the surface of the GCP@Bi_2O_3 sensor since the slope values are very close to the Nernstian theoretical value (−59 mV/pH).

Tafel patterns were analyzed to discover the potential redox mechanism of APAP at the surface of the GCP@Bi_2O_3 electrode. The Tafel region refers to the linearly increasing segment in the electrode's voltammetric response (*current*, I (A) vs. *potential*, E (V)) toward the analyte affected by electron transfer kinetics between the analyte and the electrode surface [87]. Figure S2A shows the cyclic voltammetric response of the GCP@Bi_2O_3 electrode toward 10 μM APAP in BRBS pH = 6 at a scan rate of 50 mV/s. Red- and orange-colored dots demonstrate Tafel regions for APAP oxidation and reduction peaks (Figure S2A). The number of electrons participating in redox processes can be calculated based on the slope obtained from the *E* (*V*) vs. *log I* (*A*) linear dependence. Figures S2B and S2C depict the Tafel plot of *E* (*V*) vs. *log I* (*A*) for APAP oxidation and APAP reduction peaks, respectively. Slopes of 133 mV/A (for the oxidation peak) and 118 mV/A (for the reduction peak) indicated two electrons (the theoretical value of 59 mV/A corresponds to one-electron exchange in the reaction [87]) participating in the oxidation, that is, the reduction of APAP at the electrode surface. Figure S3 gives the potential sensing mechanism of APAP at the GCP@Bi_2O_3 electrode, based on: (i) pH measurement, which concluded that an equal number of protons and electrons participate in APAP redox processes, and (ii) the Tafel plot of *E* (*V*) vs. *log I* (*A*), which indicated two electrons in the oxidation, that is, the reduction process at the electrode surface.

3.2.2. Effect of Scan Rate

Cyclic voltammetry was used to examine the effect of the scan rate on the electrochemical behavior of the working electrode in the presence of the target analyte. This experiment was performed in triplicate. The electrochemical response of the GCP@Bi_2O_3 electrode in BRBS pH = 6 towards 10 μM APAP at different scan rates (ν) is represented in Figure 4A. The current intensity of the APAP redox peaks increased continuously with the applied scan rate (Figure 4A). In addition, the peak potential of the oxidation peak shifted towards the positive potential side. In contrast, the potential of the reduction peak moved to negative potential values. Figure 4B depicts that the $I_{p(ox)}$ and $I_{p(red)}$ of APAP are linearly dependent on the square root of the scan rate ($\nu^{1/2}$), indicating a diffusion-controlled process responsible for the APAP redox processes at the electrode surface [102]. Plots of $log\ I_{p(ox)}$ vs. $log\ \nu$ and $log\ I_{p(red)}$ vs. $log\ \nu$ were constructed to confirm the process on the electrode surface. Figure 4C,D show plots of $I_{p(ox)}$ vs. $log\ \nu$ and $I_{p(red)}$ and $log\ \nu$, where linear dependences can be expressed by Equations (5) and (6), respectively, as follows:

$$\log I_{p(ox)}(A) = 0.51 \log \nu(mV/s) - 7.60\ (r = 0.998) \tag{5}$$

$$\log I_{p(red)}(A) = 0.57 \log \nu(mV/s) - 7.84\ (r = -0.998) \tag{6}$$

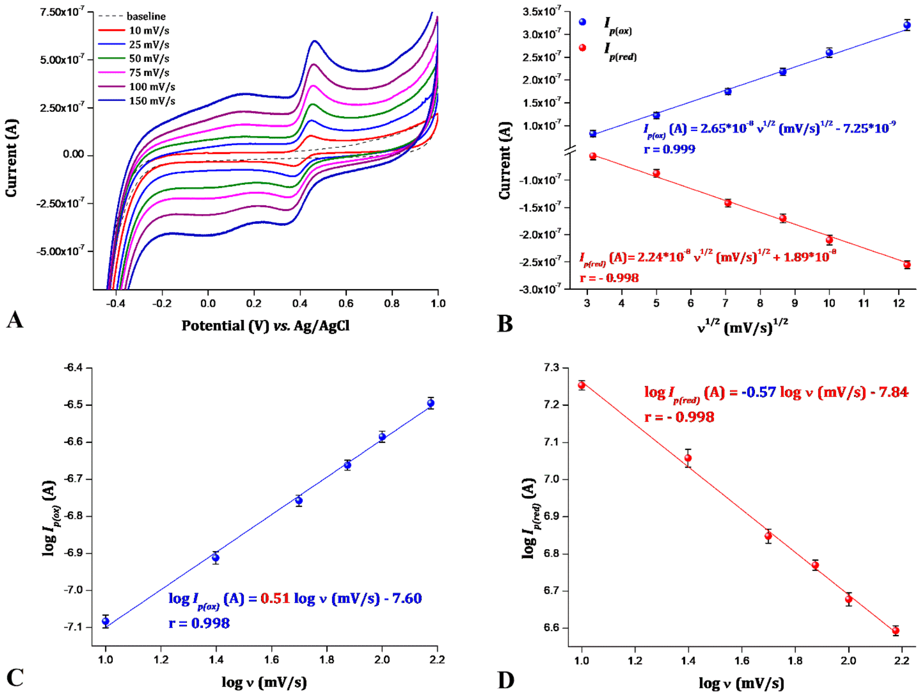

Figure 4. (**A**) Cyclic voltammetric profile of 10 μM APAP recorded at the GCP@Bi_2O_3 sensor in BRBS pH = 6 at different scan rates (10–150 mV/s). (**B**) Linear plot of I_p vs. $\nu^{1/2}$ for APAP redox peaks; (**C**) Linear plot of log $I_{p(ox)}$ vs. $log\ \nu$. (**D**) Linear plot of log $I_{p(red)}$ vs. $log\ \nu$. (**B**–**D**) show error bars representing the standard deviation between measurements (*n* = 3).

The slope of 0.51 (in the case of $I_{p(ox)}$ vs. $log\ \nu$) and 0.57 (for $I_{p(red)}$ vs. $log\ \nu$ dependence) confirms that the diffusion-controlled process is answerable for the oxidation and reduction of APAP on the surface of the GCP@Bi_2O_3 electrode due to the close values of the obtained slopes to the theoretical value of 0.5 [102]. These results comply with previously reported findings, where the authors described that the diffusion-controlled process is responsible for APAP oxidation at modified CPEs [88,89,103,104].

3.3. Voltametric Detection of the APAP at the GCP@Bi_2O_3 Sensor

An electroanalytical method for APAP detection was developed using DPV. APAP's oxidation peak was evaluated for this experiment. First, the influence of the amplitude of the DPV method on the electrochemical response of the GCP@Bi_2O_3 electrode toward the target analyte was investigated. The DPV profile of the GCP@Bi_2O_3 electrode in BRBS pH = 6 containing 5 μM APAP at different applied amplitudes (from 5 to 45 mV) is depicted in Figure S4A. Figure S4B shows an increase in $I_{p(ox)}$ with an applied amplitude up to 40 mV. A further increase in the amplitude decreases the intensity of the current signal and widens the oxidation peak (Figure S4B). Consequently, the amplitude of 40 mV was selected as optimal, and this value was used for further measurements.

The electroanalytical parameters were examined, such as the linear concentration range, the limit of detection (LOD), and the limit of quantification (LOQ). The electrochemical behavior of the GCP@Bi_2O_3 electrode was followed after successive additions of APAP standard solution (0.0050 M) in BRBS pH = 6 under the DPV method (amplitude of 40 mV, a pulse width of 0.2 s, a sampling width of 0.02 s, and a pulse period of 0.5 s). The developed sensor detected APAP in a wide concentration range from 0.05 to 12 μM (Figure 5A). The calibration was performed in triplicate. The corresponding calibration curve is depicted in Figure 5B, where error bars correspond to the standard deviation between measurements (n = 3). The linearity between $I_{p(ox)}$ and APAP concentration (C_{APAP}) is described by the equation: $I_{p(ox)}\ (A) = 0.055\ C_{APAP}\ (M) - 2.14 \times 10^{-10}$, with Pearson's coefficient (r) of 0.9996. LOQ and LOD were determined from the calibration curve as $S/N = 10$ and $S/N = 3$, respectively. LOQ was 36 nM, while LOD was calculated to be 10 nM.

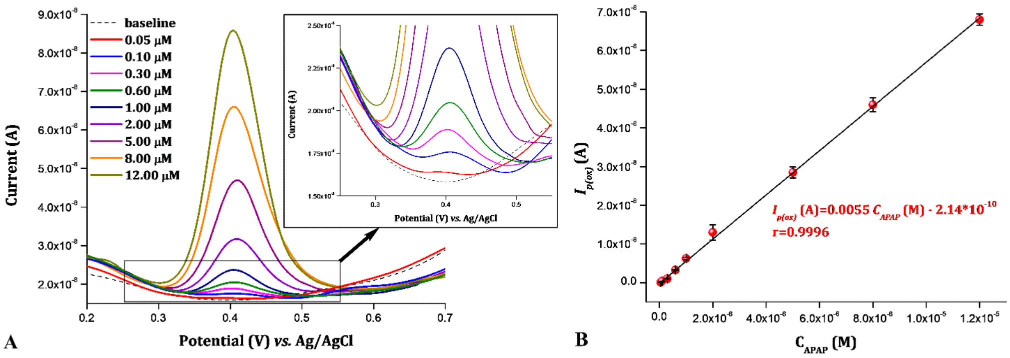

Figure 5. (**A**) DPV profiles of the GCP@Bi_2O_3 electrode for different APAP concentrations (0.05 to 12 μM) recorded in BRBS pH = 6 (DPV parameters: amplitude of 40 mV, pulse width of 0.2 s, sampling width of 0.02 s, and pulse period of 0.5 s). (**B**) Plot of $I_{p(ox)}$ vs. C_{APAP} with corresponding error bars (n = 3).

The precision and repeatability of the developed DPV method were examined using the GCP@Bi_2O_3 sensor. All measurements were performed in BRBS pH = 6. The sensor's precision was investigated by measuring the 1.0 μM APAP with three independently prepared GCP@Bi_2O_3 electrodes. The relative standard deviation (RSD) between measurements was 2.95%. The sensor's repeatability was studied by measuring three different APAP concentrations with the same GCP@Bi_2O_3 electrode in five consecutive measurements. The RSD between repetitions for APAP concentrations of 0.3 μM, 1.0 μM, and 5.0 μM were 1.75%, 1.03%, and 0.87%, respectively. These results indicated good precision and repeatability of the proposed GCP@Bi_2O_3 sensor and the developed DPV method toward the electrochemical determination of APAP. In addition, the stability of the developed sensor was examined in BRBS pH = 6 containing 1.0 µM APAP under the optimized DPV method. This test started the same day when the modified paste was prepared. The identical measurements were conducted with the same paste over 30 days (the paste was stored in the fridge at 4 °C). The APAP current signal was measured every 5 days. The changes in the current signal were not above 4%, indicating the excellent stability of the GCP@Bi_2O_3 sensor.

The electroanalytical parameters (LOD, LOQ, and linear concentration range) acquired with the GCP@Bi_2O_3 sensor were compared with identical parameters obtained with previously published carbon paste-based electrochemical sensors for APAP detection. Table 1 shows that the proposed GCP@Bi_2O_3 sensor and developed DPV method provided similar or superior properties for the given electroanalytical parameters. The advantages of the proposed electrochemical platform for APAP detection are reflected through the low-cost precursors for Bi_2O_3 synthesis, the simple and rapid synthesis of the Bi_2O_3 material, and the simple preparation of the working electrode. Additionally, the GCP@Bi_2O_3 sensor provided adequate precision, repeatability, and selectivity (see Section 3.4. Selectivity of the Developed GCP@Bi_2O_3 Sensor) toward APAP detection, indicating that the results provided by this electrochemical platform are appropriate and comparable to those previously reported.

Table 1. Comparison of electroanalytical parameters of different electrochemical sensors based on carbon paste modification with different materials previously published for APAP detection with this study.

Electrode	Technique	Linear Concentration Range (µM)	LOQ (nM)	LOD (nM)	Literature
CPE/NiZ/GO	DPV	0.026–0.795	26	7.8	[88]
CPE/safranin	CV	10–100	1580	470	[105]
CPE/GR-$CoFe_2O_4$	SWV	0.03–12.00	83	25	[89]
CPE/carbon	DPV	0.1–1000.0	n.g.	15	[103]
CPE/nevirapine	DPV	2–12	n.g.	770	[106]
CPE/GO/poly(Val)	DPV	5–60	960	290	[107]
CPE/SSW	SWV	80–1000	n.g.	5.54	[108]
CPE/RGO	SWV	1.2–220.0	930	310	[109]
CPE/MoO_3	SWV	1–15	n.g.	140	[110]
CPE/La_2O_3	SWAdV	0.99–19.00	n.g.	20	[111]
GCP/ILC	DPV	0–120	n.g.	2800	[112]
GCP/$MMTK_{10}$	DPV	1–15	n.g.	460	[113]
GCP@Bi_2O_3	DPV	0.05–12.00	36	10	This work

CPE—carbon paste electrode; CV—cyclic voltammetry; DPV—differential pulse voltammetry; GO—graphene oxide; GR—graphene; ILC—ionic liquid crystal; $MMTK_{10}$—potassium montmorillonite ($MMTK_{10}$)clay; NiZ—mesoporous natural zeolite with the introduced Ni^{2+}; poly(Val)—electropolymerized L-Valine; RGO—reduced graphene oxide; SSW—shrimp shell waste; SWAdV—square wave adsorptive voltammetry; SWV—square wave voltammetry.

3.4. Selectivity of the Developed GCP@Bi_2O_3 Sensor

A selectivity study is required to successfully apply the electrochemical sensor to real samples. Therefore, the selectivity of the developed GCP@Bi_2O_3 sensor was evaluated in the presence of different interferences that are regularly present in real samples. This experiment was performed using the optimized DPV method. The electrochemical behavior of the GCP@Bi_2O_3 electrode toward 1 µM APAP (oxidation peak was evaluated) in BRBS pH = 6 was followed in the absence and, then, the presence (successive addition) of different ions (K^+, Na^+, NO_3^-, and SO_4^{2-}), glucose (Glu), and caffeine (Caff). These compounds were selected due to the practical application of the sensor in pharmaceuticals. K^+ and Na^+ ions were applied in a concentration of 200 µM, while a concentration of NO_3^- and SO_4^{2-} was 100 µM. The concentrations of Glu and Caff in this experiment were 100 µM and 16 µM, respectively. Figure S5 depicts the peak current change (%) in the presence of a 16- to 200-fold higher concentration of interfering compounds (compared to the target analyte), where the current signal change was less than 10%. These results indicated satisfactory selectivity of the GCP@Bi_2O_3 sensor toward APAP determination. On the other hand, the selectivity of the developed sensor toward APAP is not investigated in the presence of compounds structurally analogous to APAP.

3.5. Real Sample Analysis

The practical application of the proposed GCP@Bi_2O_3 sensor and developed DPV method were examined in pharmaceuticals. The standard addition method determined APAP in three independent tablets of the Caffetin® pharmaceutical formulation. According to the manufacturer, each tablet contains 250 mg of APAP. The preparation of Caffetin® tablets is described in Section 2.2.3. Preparation of Real Samples. During electrochemical analysis, a certain amount of solution B was added to 25 mL of BRBS pH = 6, whereby the GCP@Bi_2O_3 sensor, under optimized DPV parameters, recorded the presence of APAP in the analyzed system. Further analysis was based on adding different amounts of APAP standard solution (0.0050 M) into the electrochemical cell. The final concentration of standard additions was 3.00 µM, 6.00 µM, and 8.00 µM. The APAP detection in the Caffetin® pharmaceutical formulation was performed in triplicate. Figure S6A shows the DPV responses of the GCP@Bi_2O_3 sensor during APAP detection in the pharmaceutical formulation using the standard addition method. The DP voltammograms in Figure S6A refer to the APAP analysis in tablet 2, where the final spike (sample) concentration was 1.0 µM (found value was 1.022 µM). Figure S6B provides a corresponding plot of $I_{p(ox)}$ vs. C_{APAP}. The recalculated results are summarized in Table 2. The recovery obtained between the declared APAP content and the found APAP content (Table 2) indicated favorable accuracy, precision, and applicability of the GCP@Bi_2O_3 sensor and the developed DPV method for real-time APAP detection in pharmaceuticals, with minimal influence of the matrix effect.

Table 2. Results for APAP determination in pharmaceutical formulation Caffetin® using GCP@Bi_2O_3 sensor and developed DPV method; comparison with declared value.

Pharmaceutical Formulation	Declared APAP Content (mg) [1]	Found APAP Content (mg) [2] ± SD [3]	Recovery (%) [4]
Tablet 1	250	262 ± 2	105
Tablet 2	250	257 ± 2	103
Tablet 3	250	260 ± 2	104

[1] prescribed by the manufacturer. [2] found by the proposed GCP@Bi_2O_3 sensor and the developed DPV method. [3] SD—standard deviation between repetitions (n = 3). [4] Recovery (%) was calculated as (C_{APAP} found/C_{APAP} declared) × 100.

4. Conclusions

A novel approach for synthesizing the α-Bi_2O_3 structure was employed, involving a modified reverse co-precipitation method that utilized glacial acetic acid instead of the conventionally used nitric acid. Structural and morphological characterization techniques confirmed the formation of α-Bi_2O_3 microstructure with a rod-like morphology. The synthesized α-Bi_2O_3 material was used to modify a GCP electrode to develop an electrochemical sensor to detect APAP using the DPV technique. Cyclic voltammetry studies demonstrated that the GCP@Bi_2O_3 sensor exhibited enhanced redox peak currents of APAP in BRBS pH = 3, improved reversibility, favorable conductivity at the electrode surface, increased electroactive surface area, and a higher heterogeneous electron transfer rate constant compared to the bare GCP. The favorable electrochemical performances of the GCP@Bi_2O_3 sensor toward APAP were provided in BRBS pH = 6. The scan rate study displayed a diffusion-controlled process responsible for APAP redox processes at the surface of the developed sensor. The DPV measurements showed that the GCP@Bi_2O_3 sensor detected APAP in a wide linear concentration range (0.05 to 12 µM). The LOQ and LOD of the developed electroanalytical method were 36 nM and 10 nM, respectively, indicating that the obtained findings are reliable, comparable, and/or superior to previously reported studies. The developed sensor offered adequate precision, repeatability, and selectivity toward APAP detection. The recovery tests indicated that α-Bi_2O_3 material can be used as a highly functional carbon paste modifier for real-time APAP detection in pharmaceuticals.

Supplementary Materials: The following supporting information can be downloaded at: https://www.mdpi.com/article/10.3390/chemosensors12070122/s1, Addition S1. The detailed content of Caffetin® tablets; Figure S1: EDS results of the synthesized Bi_2O_3; Figure S2: (A) Cyclic voltammetric response of the GCP@Bi_2O_3 electrode in BRBS pH = 6 containing 10 μM APAP. Scan rate of 50 mV/s. Red- and orange-colored dots demonstrate Tafel regions for APAP oxidation and reduction peak; (B) Tafel plot (E (V) vs. $log\ I_{p(ox)}$ (A)) for APAP oxidation peak; (C) Tafel plot (E (V) vs. $log\ I_{p(red)}$ (A)) for APAP reduction peak; Figure S3: Proposed redox mechanism of APAP; Figure S4: (A) DPV records of the GCP@Bi_2O_3 electrode for 5 μM APAP in BRBS pH = 6 at different amplitudes (5 to 45 mV). The other DPV parameters were a pulse width of 0.2 s, a sampling width of 0.02 s, and a pulse period of 0.5 s; (B) Plot of $I_{p(ox)}$ vs. applied amplitude with corresponding error bars (n = 3); Figure S5: Change in the APAP peak current after successive addition of investigated interferences; and Figure S6: APAP detection in Caffetin® tablet 2 using the standard addition method. (A) DPV records of the GCP@Bi_2O_3 sensor in BRBS pH = 6 for APAP detection in the pharmaceutical formulation: the concentration of the spike sample was 1.0 μM; the concentration of the first standard addition was 3.0 μM; the concentration of the second standard addition was 6.0 μM; and the concentration of the third standard addition was 8.0 μM. DPV parameters were amplitude of 40 mV, pulse width of 0.2 s, sampling width of 0.02 s, and pulse period of 0.5 s; (B) Appropriate plot of $I_{p(ox)}$ vs. C_{APAP} with corresponding error bars (n = 3); Table S1: The phase composition, unit cell, and microstructural parameters for the synthesized Bi_2O_3.

Author Contributions: Conceptualization, L.A. and M.Š.; methodology, L.A., S.Đ., D.S., A.K., V.B.P., D.A.J. and M.Š.; validation, S.Đ. and D.S.; investigation, L.A., S.Đ., D.S., A.K., V.B.P., D.A.J. and M.Š.; resources, L.A., S.Đ., D.S., A.K., V.B.P., D.A.J. and M.Š.; writing—original draft preparation, L.A., S.Đ., and M.Š.; writing—review and editing, L.A., S.Đ. and M.Š.; visualization, L.A., S.Đ. and M.Š.; supervision, M.Š.; project administration, M.Š. All authors have read and agreed to the published version of the manuscript.

Funding: This research was funded by the Ministry of Science, Technological Development and Innovation of the Republic of Serbia (Contract Nos: 451-03-47/2024-03/200026, 451-03-47/2024-03/200168, 451-03-47/2024-03/200126, 451-03-47/2024-03/200116, and 451-03-47/2024-03/200288) as well as by the University of Belgrade—Institute of Chemistry, Technology and Metallurgy through the “Seed Research Grant” for young scientists (“Synthesis of bismuth oxide polymorphs: From simple particles to multidimensional structures, SynBiOmorph”), financed by the Serbia Accelerating Innovation and Entrepreneurship Project (SAIGE).

Informed Consent Statement: Not applicable.

Data Availability Statement: All created data are included in the manuscript.

Conflicts of Interest: The authors declare no conflicts of interest.

References

1. Cernat, A.; Tertiş, M.; Săndulescu, R.; Bedioui, F.; Cristea, A.; Cristea, C. Electrochemical Sensors Based on Carbon Nanomaterials for Acetaminophen Detection: A Review. *Anal. Chim. Acta* **2015**, *886*, 16–28. [CrossRef] [PubMed]
2. Aminoshariae, A.; Khan, A. Acetaminophen: Old Drug, New Issues. *J. Endod.* **2015**, *41*, 588–593. [CrossRef]
3. Gupta, A.; Jakobsson, J. Acetaminophen, Nonsteroidal Anti-Inflammatory Drugs, and Cyclooxygenase-2 Selective Inhibitors: An Update. *Plast. Reconstr. Surg.* **2014**, *134*, 24S–31S. [CrossRef]
4. Jaeschke, H. Role of Inflammation in the Mechanism of Acetaminophen-Induced Hepatotoxicity. *Expert Opin. Drug Metab. Toxicol.* **2005**, *1*, 389–397. [CrossRef]
5. James, L.P.; Mayeux, P.R.; Hinson, J.A. Acetaminophen-induced hepatotoxicity. *Drug Metab. Dispos.* **2003**, *31*, 1499. [CrossRef] [PubMed]
6. Yoon, E.; Babar, A.; Choudhary, M.; Kutner, M.; Pyrsopoulos, N. Acetaminophen-Induced Hepatotoxicity: A Comprehensive Update. *J. Clin. Transl. Hepatol.* **2016**, *4*, 131–142. [CrossRef] [PubMed]
7. Montaseri, H.; Forbes, P.B.C. Analytical Techniques for the Determination of Acetaminophen: A Review. *TrAC Trends Anal. Chem.* **2018**, *108*, 122–134. [CrossRef]

8. Campanero, M.A.; Calahorra, B.; García-Quétglas, E.; López-Ocáriz, A.; Honorato, J. Rapid Liquid Chromatographic Assay for the Determination of Acetaminophen in Plasma after Propacetamol Administration: Application to Pharmacokinetic Studies. *J. Pharm. Biomed. Anal.* **1999**, *20*, 327–334. [CrossRef]
9. Gioia, M.G.; Andreatta, P.; Boschetti, S.; Gatti, R. Development and Validation of a Liquid Chromatographic Method for the Determination of Ascorbic Acid, Dehydroascorbic Acid and Acetaminophen in Pharmaceuticals. *J. Pharm. Biomed. Anal.* **2008**, *48*, 331–339. [CrossRef]
10. Mrochek, J.E.; Katz, S.; Christie, W.H.; Dinsmore, S.R. Acetaminophen Metabolism in Man, as Determined by High-Resolution Liquid Chromatography. *Clin. Chem.* **1974**, *20*, 1086–1096. [CrossRef]
11. Kamberi, M.; Riley, C.M.; Ma (Sharon), X.; Huang, C.-W.C. A Validated, Sensitive HPLC Method for the Determination of Trace Impurities in Acetaminophen Drug Substance. *J. Pharm. Biomed. Anal.* **2004**, *34*, 123–128. [CrossRef] [PubMed]
12. Săndulescu, R.; Mirel, S.; Oprean, R. The Development of Spectrophotometric and Electroanalytical Methods for Ascorbic Acid and Acetaminophen and Their Applications in the Analysis of Effervescent Dosage Forms. *J. Pharm. Biomed. Anal.* **2000**, *23*, 77–87. [CrossRef] [PubMed]
13. Afshari, J.T.; Liu, T.-Z. Rapid Spectrophotometric Method for the Quantitation of Acetaminophen in Serum. *Anal. Chim. Acta* **2001**, *443*, 165–169. [CrossRef]
14. Souri, E.; Nasab, S.A.M.; Amanlou, M.; Tehrani, M.B. Development and Validation of a Rapid Derivative Spectrophotometric Method for Simultaneous Determination of Acetaminophen, Ibuprofen and Caffeine. *J. Anal. Chem.* **2015**, *70*, 333–338. [CrossRef]
15. Mokhtari, A.; Jafari Delouei, N.; Keyvanfard, M.; Abdolhosseini, M. Multiway Analysis Applied to Time-Resolved Chemiluminescence for Simultaneous Determination of Paracetamol and Codeine in Pharmaceuticals. *Luminescence* **2016**, *31*, 1267–1276. [CrossRef] [PubMed]
16. Ruengsitagoon, W.; Liawruangrath, S.; Townshend, A. Flow Injection Chemiluminescence Determination of Paracetamol. *Talanta* **2006**, *69*, 976–983. [CrossRef] [PubMed]
17. Wu, Y.; Zhang, H.; Yu, S.; Yu, F.; Li, Y.; Zhang, H.; Qu, L.; Harrington, P.d.B. Study on the Reaction Mechanism and the Static Injection Chemiluminescence Method for Detection of Acetaminophen. *Luminescence* **2013**, *28*, 905–909. [CrossRef] [PubMed]
18. Burgot, G.; Auffret, F.; Burgot, J.-L. Determination of Acetaminophen by Thermometric Titrimetry. *Anal. Chim. Acta* **1997**, *343*, 125–128. [CrossRef]
19. Relli-Dempsey, V.M.T. A Thermometric Titration Study of Acetaminophen and Sodium Hypochlorite. Ohio Dominican University, Columbus, OH, USA. 2018. Available online: https://etd.ohiolink.edu/acprod/odb_etd/etd/r/1501/10?clear=10&p10_accession_num=oduhonors152621864170557 (accessed on 26 June 2024).
20. Chu, Q.; Jiang, L.; Tian, X.; Ye, J. Rapid Determination of Acetaminophen and P-Aminophenol in Pharmaceutical Formulations Using Miniaturized Capillary Electrophoresis with Amperometric Detection. *Anal. Chim. Acta* **2008**, *606*, 246–251. [CrossRef]
21. He, F.Y.; Liu, A.L.; Xia, X.H. Poly(Dimethylsiloxane) Microchip Capillary Electrophoresis with Electrochemical Detection for Rapid Measurement of Acetaminophen and Its Hydrolysate. *Anal. Bioanal. Chem.* **2004**, *379*, 1062–1067. [CrossRef]
22. Lecoeur, M.; Rabenirina, G.; Schifano, N.; Odou, P.; Ethgen, S.; Lebuffe, G.; Foulon, C. Determination of Acetaminophen and Its Main Metabolites in Urine by Capillary Electrophoresis Hyphenated to Mass Spectrometry. *Talanta* **2019**, *205*, 120108. [CrossRef] [PubMed]
23. Abdel-Wadood, H.M.; Mohamed, N.A.; Mohamed, F.A. Spectrofluorimetric Determination of Acetaminophen with N-Bromosuccinimide. *J. AOAC Int.* **2005**, *88*, 1626–1630. [CrossRef] [PubMed]
24. Ahmed, M.J. A Highly Selective and Sensitive Spectrofluorimetric Method for the Determination of N-Acetyl-4-Aminophenol at Nano-Trace Levels in Pharmaceuticals and Biological Fluids Using Cerium (IV). *Pak. J. Anal. Environ. Chem.* **2019**, *20*, 17–31. [CrossRef]
25. de los, A.; Oliva, M.; Olsina, R.A.; Masi, A.N. Selective Spectrofluorimetric Method for Paracetamol Determination through Coumarinic Compound Formation. *Talanta* **2005**, *66*, 229–235. [CrossRef]
26. Lee, S.H.; Lee, J.H.; Tran, V.-K.; Ko, E.; Park, C.H.; Chung, W.S.; Seong, G.H. Determination of Acetaminophen Using Functional Paper-Based Electrochemical Devices. *Sens. Actuators B Chem.* **2016**, *232*, 514–522. [CrossRef]
27. Beitollahi, H.; Raoof, J.-B.; Hosseinzadeh, R. Fabrication of a Nanostructure-Based Electrochemical Sensor for Simultaneous Determination of N-Acetylcysteine and Acetaminophen. *Talanta* **2011**, *85*, 2128–2134. [CrossRef] [PubMed]
28. Adhikari, B.-R.; Govindhan, M.; Chen, A. Sensitive Detection of Acetaminophen with Graphene-Based Electrochemical Sensor. *Electrochim. Acta* **2015**, *162*, 198–204. [CrossRef]
29. Kumari, L.; Lin, J.-H.; Ma, Y.-R. One-Dimensional Bi_2O_3 Nanohooks: Synthesis, Characterization and Optical Properties. *J. Phys. Condens. Matter* **2007**, *19*, 406204. [CrossRef] [PubMed]
30. Zhou, L.; Wang, W.; Xu, H.; Sun, S.; Shang, M. Bi_2O_3 Hierarchical Nanostructures: Controllable Synthesis, Growth Mechanism, and Their Application in Photocatalysis. *Chem.—A Eur. J.* **2009**, *15*, 1776–1782. [CrossRef]
31. Shinde, P.V.; Shinde, N.M.; Shaikh, S.F.; Lee, D.; Yun, J.M.; Woo, L.J.; Al-Enizi, A.M.; Mane, R.S.; Kim, K.H. Room-Temperature Synthesis and CO_2-Gas Sensitivity of Bismuth Oxide Nanosensors. *RSC Adv.* **2020**, *10*, 17217–17227. [CrossRef]
32. Hao, C.; Shen, Y.; Shen, J.; Xu, K.; Wang, X.; Zhao, Y.; Ge, C. A Glassy Carbon Electrode Modified with Bismuth Oxide Nanoparticles and Chitosan as a Sensor for Pb(II) and Cd(II). *Microchim. Acta* **2016**, *183*, 1823–1830. [CrossRef]

33. Kokulnathan, T.; Vishnuraj, R.; Wang, T.-J.; Kumar, E.A.; Pullithadathil, B. Heterostructured Bismuth Oxide/Hexagonal-Boron Nitride Nanocomposite: A Disposable Electrochemical Sensor for Detection of Flutamide. *Ecotoxicol. Environ. Saf.* **2021**, *207*, 111276. [CrossRef] [PubMed]
34. Cabot, A.; Marsal, A.; Arbiol, J.; Morante, J.R. Bi_2O_3 as a Selective Sensing Material for NO Detection. *Sens. Actuators B Chem.* **2004**, *99*, 74–89. [CrossRef]
35. Bhande, S.S.; Mane, R.S.; Ghule, A.V.; Han, S.-H. A Bismuth Oxide Nanoplate-Based Carbon Dioxide Gas Sensor. *Scr. Mater.* **2011**, *65*, 1081–1084. [CrossRef]
36. Leontie, L.; Caraman, M.; Visinoiu, A.; Rusu, G.I. On the Optical Properties of Bismuth Oxide Thin Films Prepared by Pulsed Laser Deposition. *Thin Solid Film.* **2005**, *473*, 230–235. [CrossRef]
37. Leontie, L.; Caraman, M.; Delibaş, M.; Rusu, G.I. Optical Properties of Bismuth Trioxide Thin Films. *Mater. Res. Bull.* **2001**, *36*, 1629–1637. [CrossRef]
38. Mahmoud, W.E.; Al-Ghamdi, A.A. Synthesis and Properties of Bismuth Oxide Nanoshell Coated Polyaniline Nanoparticles for Promising Photovoltaic Properties. *Polym. Adv. Technol.* **2011**, *22*, 877–881. [CrossRef]
39. Park, J.-Y.; Wachsman, E.D. Stable and High Conductivity Ceria/Bismuth Oxide Bilayer Electrolytes for Lower Temperature Solid Oxide Fuel Cells. *Ionics* **2006**, *12*, 15–20. [CrossRef]
40. Sarat, S.; Sammes, N.; Smirnova, A. Bismuth Oxide Doped Scandia-Stabilized Zirconia Electrolyte for the Intermediate Temperature Solid Oxide Fuel Cells. *J. Power Sources* **2006**, *160*, 892–896. [CrossRef]
41. Azad, A.M.; Larose, S.; Akbar, S.A. Bismuth Oxide-Based Solid Electrolytes for Fuel Cells. *J. Mater. Sci.* **1994**, *29*, 4135–4151. [CrossRef]
42. Mohd Suib, N.R.; Nur-Akasyah, J.; Muhammad Aizat, K.; Abd-Shukor, R. Electrical Properties of Nano Bi_2O_3 Added (Bi,Pb)Sr-Ca-Cu-O Superconductor. *J. Phys. Conf. Ser.* **2018**, *1083*, 12045. [CrossRef]
43. Koza, J.A.; Bohannan, E.W.; Switzer, J.A. Superconducting Filaments Formed During Nonvolatile Resistance Switching in Electrodeposited δ-Bi_2O_3. *ACS Nano* **2013**, *7*, 9940–9946. [CrossRef]
44. Majewski, P. Materials Aspects of the High-Temperature Superconductors in the System Bi_2O_3–SrO–CaO–CuO. *J. Mater. Res.* **2000**, *15*, 854–870. [CrossRef]
45. Tran-Phu, T.; Daiyan, R.; Fusco, Z.; Ma, Z.; Amal, R.; Tricoli, A. Nanostructured β-Bi_2O_3 Fractals on Carbon Fibers for Highly Selective CO_2 Electroreduction to Formate. *Adv. Funct. Mater.* **2020**, *30*, 1906478. [CrossRef]
46. Yang, Z.; Wang, H.; Bi, X.; Tan, X.; Zhao, Y.; Wang, W.; Zou, Y.; Wang, H.; Ning, H.; Wu, M. Bimetallic In_2O_3/Bi_2O_3 Catalysts Enable Highly Selective CO_2 Electroreduction to Formate within Ultra-Broad Potential Windows. *Energy Environ. Mater.* **2022**, *7*, e12508. [CrossRef]
47. Yasuda, K.; Nobu, M.; Masui, T.; Imanaka, N. Complete Oxidation of Acetaldehyde on Pt/CeO_2–ZrO_2– Bi_2O_3 Catalysts. *Mater. Res. Bull.* **2010**, *45*, 1278–1282. [CrossRef]
48. Jiang, H.-Y.; Liu, J.; Cheng, K.; Sun, W.; Lin, J. Enhanced Visible Light Photocatalysis of Bi_2O_3 upon Fluorination. *J. Phys. Chem. C* **2013**, *117*, 20029–20036. [CrossRef]
49. Sun, C.; Liu, J.; Li, L.; Cheng, J.; Peng, Y.; Xie, Q. Photoanode Synthesis of Ammonia Based on a Light Reflex Strategy and NiCe-Layered Double Hydroxide and Oxygen-Vacancy Bi_2O_3 Catalysts. *Chem. Eng. J.* **2023**, *464*, 142447. [CrossRef]
50. Pugazhenthiran, N.; Sathishkumar, P.; Murugesan, S.; Anandan, S. Effective Degradation of Acid Orange 10 by Catalytic Ozonation in the Presence of Au- Bi_2O_3 Nanoparticles. *Chem. Eng. J.* **2011**, *168*, 1227–1233. [CrossRef]
51. Irmawati, R.; Noorfarizan Nasriah, M.N.; Taufiq-Yap, Y.H.; Abdul Hamid, S.B. Characterization of Bismuth Oxide Catalysts Prepared from Bismuth Trinitrate Pentahydrate: Influence of Bismuth Concentration. *Catal. Today* **2004**, *93–95*, 701–709. [CrossRef]
52. Abu-Dief, A.M.; Mohamed, W.S. α-Bi_2O_3 Nanorods: Synthesis, Characterization and UV-Photocatalytic Activity. *Mater. Res. Express* **2017**, *4*, 35039. [CrossRef]
53. Li, L.; Tao, R.; Liu, Y.; Zhou, K.; Fan, X.; Han, Y.; Tang, L. Co_3O_4 Nanoparticles/Bi_2O_3 Nanosheets: One Step Synthesis, High-Efficiency Thermal Catalytic Performance, and Catalytic Mechanism Research. *Mol. Catal.* **2022**, *528*, 112483. [CrossRef]
54. Liang, Z.; Cao, Y.; Li, Y.; Xie, J.; Guo, N.; Jia, D. Solid-State Chemical Synthesis of Rod-like Fluorine-Doped β-Bi_2O_3 and Their Enhanced Photocatalytic Property under Visible Light. *Appl. Surf. Sci.* **2016**, *390*, 78–85. [CrossRef]
55. Wang, C.; Shao, C.; Wang, L.; Zhang, L.; Li, X.; Liu, Y. Electrospinning Preparation, Characterization and Photocatalytic Properties of Bi_2O_3 Nanofibers. *J. Colloid Interface Sci.* **2009**, *333*, 242–248. [CrossRef] [PubMed]
56. Wu, C.; Shen, L.; Huang, Q.; Zhang, Y.-C. Hydrothermal Synthesis and Characterization of Bi_2O_3 Nanowires. *Mater. Lett.* **2011**, *65*, 1134–1136. [CrossRef]
57. Zhang, G.; Zhang, X.; Wu, Y.; Shi, W.; Guan, W. Rapid Microwave-Assisted Synthesis of Bi_2O_3 Tubes and Photocatalytic Properties for Antibiotics. *Micro Nano Lett.* **2013**, *8*, 177–180. [CrossRef]
58. Venegas-Castro, A.; Reyes-Contreras, A.; Camacho-López, M.; Olea-Mejía, O.; Camacho-López, S.; Esparza-García, A. Study of the Integrated Fluence Threshold Condition for the Formation of β-Bi_2O_3 on Bi Thin Films by Using Ns Laser Pulses. *Opt. Laser Technol.* **2016**, *81*, 50–54. [CrossRef]
59. Janardhana, D.; Jayaramu, S.N.; Roos, W.D.; Purcell, W.; Swart, H.C. Influences of Substrate Temperatures and Oxygen Partial Pressures on the Crystal Structure, Morphology and Luminescence Properties of Pulsed Laser Deposited Bi_2O_3:Ho^{3+} Thin Films. *Coatings* **2020**, *10*, 1168. [CrossRef]

60. Zhu, B.L.; Zhao, X.Z. Study on Structure and Optical Properties of Bi_2O_3 Thin Films Prepared by Reactive Pulsed Laser Deposition. *Opt. Mater.* **2006**, *29*, 192–198. [CrossRef]
61. Divya, J.; Shivaramu, N.J.; Swart, H.C. Heliyon Thin Films Deposited by Pulsed Laser Deposition for Improved Green and Near-Infrared Emissions and Photocatalytic Activity. *Heliyon* **2024**, *10*, e23200. [CrossRef]
62. Zhou, L.; Xie, M.; Su, H.; Chen, R.; Pang, Y.; Lou, H.; Yang, D.; Qiu, X. In Situ Oxidation of Ethylene Glycol Coupled with Bi_2O_3 Epitaxial Growth to Prepare Bi_2O_3/BiOCOOH Heterojunctions with Oxygen Vacancies for Efficient Photocatalytic Lignin Degradation. *Colloids Surf. A Physicochem. Eng. Asp.* **2023**, *664*, 131134. [CrossRef]
63. Proffit, D.L.; Bai, G.-R.; Fong, D.D.; Fister, T.T.; Hruszkewycz, S.O.; Highland, M.J.; Baldo, P.M.; Fuoss, P.H.; Mason, T.O.; Eastman, J.A. Phase Stabilization of δ-Bi_2O_3 Nanostructures by Epitaxial Growth onto Single Crystal $SrTiO_3$ or $DyScO_3$ Substrates. *Appl. Phys. Lett.* **2010**, *96*, 21905. [CrossRef]
64. Xu, J.; Liu, J. Facet-Selective Epitaxial Growth of δ-Bi_2O_3 on ZnO Nanowires. *Chem. Mater.* **2016**, *28*, 8141–8148. [CrossRef]
65. Wang, L.; Cui, Z.-L.; Zhang, Z.-K. Bi Nanoparticles and Bi_2O_3 Nanorods Formed by Thermal Plasma and Heat Treatment. *Surf. Coat. Technol.* **2007**, *201*, 5330–5332. [CrossRef]
66. Iljinas, A.; Marcinauskas, L. Formation of Bismuth Oxide Nanostructures by Reactive Plasma Assisted Thermal Evaporation. *Thin Solid Film.* **2015**, *594*, 192–196. [CrossRef]
67. Tien, L.-C.; Liou, Y.-H. Synthesis of Bi_2O_3 Nanocones over Large Areas by Magnetron Sputtering. *Surface and Coatings Technology* **2015**, *265*, 1–6. [CrossRef]
68. Lunca Popa, P.; Sønderby, S.; Kerdsongpanya, S.; Lu, J.; Bonanos, N.; Eklund, P. Highly Oriented δ-Bi_2O_3 Thin Films Stable at Room Temperature Synthesized by Reactive Magnetron Sputtering. *J. Appl. Phys.* **2013**, *113*, 46101. [CrossRef]
69. Tien, L.-C.; Lai, Y.-C. Nucleation Control and Growth Mechanism of Pure α-Bi_2O_3 Nanowires. *Appl. Surf. Sci.* **2014**, *290*, 131–136. [CrossRef]
70. Ho, C.-H.; Chan, C.-H.; Huang, Y.-S.; Tien, L.-C.; Chao, L.-C. The Study of Optical Band Edge Property of Bismuth Oxide Nanowires α-Bi_2O_3. *Opt. Express* **2013**, *21*, 11965–11972. [CrossRef]
71. Ma, H.; Yang, X.; Tang, X.; Cao, X.; Dai, R. Self-Assembled Co-Doped β-Bi_2O_3 Flower-like Structure for Enhanced Photocatalytic Antibacterial Effect under Visible Light. *Appl. Surf. Sci.* **2022**, *572*, 151348. [CrossRef]
72. Lee, K.T.; Lidie, A.A.; Jeon, S.Y.; Hitz, G.T.; Song, S.J.; Wachsman, E.D. Highly Functional Nano-Scale Stabilized Bismuth Oxides via Reverse Strike Co-Precipitation for Solid Oxide Fuel Cells. *J. Mater. Chem. A* **2013**, *1*, 6199–6207. [CrossRef]
73. Labib, S. Preparation, Characterization and Photocatalytic Properties of Doped and Undoped Bi_2O_3. *J. Saudi Chem. Soc.* **2017**, *21*, 664–672. [CrossRef]
74. Cao, S.; Chen, C.; Xie, X.; Zeng, B.; Ning, X.; Liu, T.; Chen, X.; Meng, X.; Xiao, Y. Hypothermia-Controlled Co-Precipitation Route to Deposit Well-Dispersed β-Bi_2O_3 Nanospheres on Polymorphic Graphene Flakes. *Vacuum* **2014**, *102*, 1–4. [CrossRef]
75. Qiao, J.; Chen, K.; Li, S.; Liu, Y.; Cao, H.; Wei, G.; Kong, L.; Zhang, X.; Liu, H. Plasma Spray–Chemical Vapor Deposition of Nanotextured Film with α/β Bi_2O_3 Heterostructure and Photocatalytic Degradation Performance. *Vacuum* **2021**, *188*, 110206. [CrossRef]
76. Kim, H.W.; Myung, J.H.; Shim, S.H. One-Dimensional Structures of Bi_2O_3 Synthesized via Metalorganic Chemical Vapor Deposition Process. *Solid State Commun.* **2006**, *137*, 196–198. [CrossRef]
77. Shen, X.-P.; Wu, S.-K.; Zhao, H.; Liu, Q. Synthesis of Single-Crystalline Bi_2O_3 Nanowires by Atmospheric Pressure Chemical Vapor Deposition Approach. *Phys. E Low-Dimens. Syst. Nanostructures* **2007**, *39*, 133–136. [CrossRef]
78. Azizian-Kalandaragh, Y.; Sedaghatdoust-Bodagh, F.; Habibi-Yangjeh, A. Ultrasound-Assisted Preparation and Characterization of β-Bi_2O_3 Nanostructures: Exploring the Photocatalytic Activity against Rhodamine B. *Superlattices Microstruct.* **2015**, *81*, 151–160. [CrossRef]
79. Manjula, N.; Chen, T.-W.; Chen, S.-M.; Lou, B.-S. Sonochemical Synthesis and Characterization of Rod-Shaped Bi_2O_3/ZnO Anchored with f-MWCNT Nanocomposite for the Electrochemical Determination of Ofloxacin. *J. Electrochem. Soc.* **2021**, *168*, 87506. [CrossRef]
80. Kusuma, K.B.; Manju, M.; Ravikumar, C.R.; Dileepkumar, V.G.; Kumar, A.N.; Santosh, M.S.; Murthy, H.C.A.; Gurushantha, K. Probe Sonicated Synthesis of Bismuth Oxide (Bi_2O_3): Photocatalytic Application and Electrochemical Sensing of Ascorbic Acid and Lead. *J. Nanomater.* **2022**, *2022*, 3256611. [CrossRef]
81. Zhang, L.; Wang, W.; Yang, J.; Chen, Z.; Zhang, W.; Zhou, L.; Liu, S. Sonochemical Synthesis of Nanocrystallite Bi_2O_3 as a Visible-Light-Driven Photocatalyst. *Appl. Catal. A Gen.* **2006**, *308*, 105–110. [CrossRef]
82. Huang, Y.; Qin, J.; Hu, C.; Liu, X.; Wei, D.; Seo, H.J. Cs-Doped α-Bi_2O_3 Microplates: Hydrothermal Synthesis and Improved Photochemical Activities. *Appl. Surf. Sci.* **2019**, *473*, 401–408. [CrossRef]
83. Malligavathy, M.; Pathinettam Padiyan, D. Role of pH in the Hydrothermal Synthesis of Phase Pure Alpha Bi_2O_3 Nanoparticles and Its Structural Characterization. *Adv. Mater. Proc.* **2017**, *2*, 51–55. [CrossRef]
84. Huang, Y.; Qin, J.; Liu, X.; Wei, D.; Seo, H.J. Hydrothermal Synthesis of Flower-like Na-Doped α-Bi_2O_3 and Improved Photocatalytic Activity via the Induced Oxygen Vacancies. *J. Taiwan Inst. Chem. Eng.* **2019**, *96*, 353–360. [CrossRef]
85. Xiao, Z.; Zhong, J.; Li, J.; Huang, S.; Zeng, J.; Li, M.; Yong, G. Enhanced Photocatalytic Activity of Y and Pd-Co-Doped Bi_2O_3 Prepared by Parallel Flow Co-Precipitation Method. *J. Adv. Oxid. Technol.* **2014**, *17*, 139–144. [CrossRef]
86. Sun, W.; Wang, M.; Chen, Y.; Zhang, H. Structure and Electric Conductivity of Ce-Doped Bi_2O_3 Electrolyte Synthesized by Reverse Titration Chemical Coprecipitation. *J. Wuhan Univ. Technol.-Mater. Sci. Ed.* **2018**, *33*, 1056–1061. [CrossRef]

87. Đurđić, S.; Vlahović, F.; Ognjanović, M.; Gemeiner, P.; Sarakhman, O.; Stanković, V.; Mutić, J.; Stanković, D.; Švorc, L'. Nano-Size Cobalt-Doped Cerium Oxide Particles Embedded into Graphitic Carbon Nitride for Enhanced Electrochemical Sensing of Insecticide Fenitrothion in Environmental Samples: An Experimental Study with the Theoretical Elucidation of Redox Events. *Sci. Total Environ.* **2024**, *909*, 168483. [CrossRef]
88. Porada, R.; Wenninger, N.; Bernhart, C.; Fendrych, K.; Kochana, J.; Baś, B.; Kalcher, K.; Ortner, A. Targeted Modification of the Carbon Paste Electrode by Natural Zeolite and Graphene Oxide for the Enhanced Analysis of Paracetamol. *Microchem. J.* **2023**, *187*, 108455. [CrossRef]
89. Afkhami, A.; Khoshsafar, H.; Bagheri, H.; Madrakian, T. Facile Simultaneous Electrochemical Determination of Codeine and Acetaminophen in Pharmaceutical Samples and Biological Fluids by Graphene–$CoFe_2O_4$ Nancomposite Modified Carbon Paste Electrode. *Sens. Actuators B Chem.* **2014**, *203*, 909–918. [CrossRef]
90. Chen, M.-S.; Chen, S.-H.; Lai, F.-C.; Chen, C.-Y.; Hsieh, M.-Y.; Chang, W.-J.; Yang, J.-C.; Lin, C.-K. Sintering Temperature-Dependence on Radiopacity of $Bi_{(2-x)}Zr_xO_{(3+x/2)}$ Powders Prepared by Sol-Gel Process. *Materials* **2018**, *11*, 1685. [CrossRef]
91. Shan, D.; Zhang, J.; Xue, H.-G.; Zhang, Y.-C.; Cosnier, S.; Ding, S.-N. Polycrystalline Bismuth Oxide Films for Development of Amperometric Biosensor for Phenolic Compounds. *Biosens. Bioelectron.* **2009**, *24*, 3671–3676. [CrossRef]
92. Kohan, E.; Shiralizadeh Dezfuli, A. Environmentally Friendly Decolorization of Textile Dye C.I. Yellow 28 in Water by $Bi_{2-x}(Lu, Er)_xO_3$ Nanoparticles. *J. Mater. Sci. Mater. Electron.* **2019**, *30*, 17170–17180. [CrossRef]
93. Yang, J.; Xie, T.; Liu, C.; Xu, L. Facile Fabrication of Dumbbell-Like β-Bi_2O_3/Graphene Nanocomposites and Their Highly Efficient Photocatalytic Activity. *Materials* **2018**, *11*, 1359. [CrossRef] [PubMed]
94. Szaller, Z.; Kovács, L.; Pöppl, L. Comparative Study of Bismuth Tellurites by Infrared Absorption Spectroscopy. *J. Solid State Chem.* **2000**, *152*, 392–396. [CrossRef]
95. Yada, M.; Yamanoi, T.; Watari, T. Simple Template-Free Synthesis of Bi_2O_3 Microflowers Composed of Nanorods. *Adv. Mater. Phys. Chem.* **2020**, *10*, 319–327. [CrossRef]
96. Đurđić, S.; Ognjanović, M.; Ristivojević, M.K.; Antić, B.; Veličković, T.Ć.; Mutić, J.; Kónya, Z.; Stanković, D. Voltammetric Immunoassay Based on MWCNTs@$Nd(OH)_3$-BSA-Antibody Platform for Sensitive BSA Detection. *Microchim. Acta* **2022**, *189*, 422. [CrossRef]
97. Hasan, I.M.A.; Abd-Elsabour, M.; Assaf, F.H.; Abd-Elsabur, K.M. Green Synthesized SiO_2/Bi_2O_3 Nanocomposite Sensor for Catechol and Hydroquinone Detection in Water. *Sens. Actuators A Phys.* **2024**, *372*, 115310. [CrossRef]
98. Švancara, I.; Sýs, M.; Metelka, R.; Mikysek, T. Carbon Paste Electrodes in Laboratory Exercises for Students. *J. Solid State Electrochem.* **2024**, *28*, 1341–1360. [CrossRef]
99. Sinha, G.N.; Subramanyam, P.; Sivaramakrishna, V.; Subrahmanyam, C. Electrodeposited Copper Bismuth Oxide as a Low-Cost, Non-Enzymatic Electrochemical Sensor for Sensitive Detection of Uric Acid and Hydrogen Peroxide. *Inorg. Chem. Commun.* **2021**, *129*, 108627. [CrossRef]
100. Ansari, S.; Ansari, M.S.; Satsangee, S.P.; Jain, R. Bi_2O_3/ZnO Nanocomposite: Synthesis, Characterizations and Its Application in Electrochemical Detection of Balofloxacin as an Anti-Biotic Drug. *J. Pharm. Anal.* **2021**, *11*, 57–67. [CrossRef]
101. Hernández-Ramírez, D.; Mendoza-Huizar, L.H.; Galán-Vidal, C.A.; Aguilar-Lira, G.Y.; Rebolledo-Perales, L.E.; Álvarez-Romero, G.A. An Optimized Electrochemical Methodology by Box-Behnken Design for Non-Enzymatic Determination of Uric Acid in Urine Samples Using a Bi_2O_3 Nanoparticles-Carbon Paste Electrode. *J. Anal. Chem.* **2023**, *78*, 1557–1565. [CrossRef]
102. Jevtić, S.; Vukojević, V.; Djurdjić, S.; Pergal, M.V.; Manojlović, D.D.; Petković, B.B.; Stanković, D.M. First Electrochemistry of Herbicide Pethoxamid and Its Quantification Using Electroanalytical Approach from Mixed Commercial Product. *Electrochim. Acta* **2018**, *277*, 136–142. [CrossRef]
103. Amiri, M.; Rezapour, F.; Bezaatpour, A. Hydrophilic Carbon Nanoparticulates at the Surface of Carbon Paste Electrode Improve Determination of Paracetamol, Phenylephrine and Dextromethorphan. *J. Electroanal. Chem.* **2014**, *735*, 10–18. [CrossRef]
104. Atta, N.F.; El-Ads, E.H.; Hassan, S.H.; Galal, A. Surface Modification of Carbon Paste Electrode with Nano-Structured Modifiers: Application for Sub-Nano-Sensing of Paracetamol. *J. Electrochem. Soc.* **2017**, *164*, B519. [CrossRef]
105. Chetankumar, K.; Kumara Swamy, B.E.; Sharma, S.C. Safranin Amplified Carbon Paste Electrode Sensor for Analysis of Paracetamol and Epinephrine in Presence of Folic Acid and Ascorbic Acid. *Microchem. J.* **2021**, *160*, 105729. [CrossRef]
106. Tanuja, S.B.; Kumara Swamy, B.E.; Pai, K.V. Electrochemical Determination of Paracetamol in Presence of Folic Acid at Nevirapine Modified Carbon Paste Electrode: A Cyclic Voltammetric Study. *J. Electroanal. Chem.* **2017**, *798*, 17–23. [CrossRef]
107. Venu Gopal, T.; Reddy, T.M.; Venkataprasad, G.; Shaikshavalli, P.; Gopal, P. Rapid and Sensitive Electrochemical Monitoring of Paracetamol and Its Simultaneous Resolution in Presence of Epinephrine and Tyrosine at GO/Poly(Val) Composite Modified Carbon Paste Electrode. *Colloids Surf. A Physicochem. Eng. Asp.* **2018**, *545*, 117–126. [CrossRef]
108. Achache, M.; Elouilali Idrissi, G.; Ben Seddik, N.; El Boumlasy, S.; Kouda, I.; Raissouni, I.; Chaouket, F.; Draoui, K.; Bouchta, D.; Choukairi, M. Innovative Use of Shrimp Shell Powder in Carbon Paste Electrode for the Electrochemical Detection of Dopamine and Paracetamol: Valorization, Characterization and Application. *Microchem. J.* **2024**, *202*, 110754. [CrossRef]
109. Farag, A.S. Voltammetric Determination of Acetaminophen in Pharmaceutical Preparations and Human Urine Using Glassy Carbon Paste Electrode Modified with Reduced Graphene Oxide. *Anal. Sci.* **2022**, *38*, 1213–1220. [CrossRef]
110. Nagles, E.; Ceroni, M.; Villanueva Huerta, C.; Hurtado, J.J. Simultaneous Electrochemical Determination of Paracetamol and Allura Red in Pharmaceutical Doses and Food Using a Mo(VI) Oxide-Carbon Paste Microcomposite. *Electroanalysis* **2021**, *33*, 2335–2344. [CrossRef]

111. Nagles, E.; Ceroni, M.; Hurtado-Murillo, J.J.; Hurtado, J.J. Electrochemical Determination of Paracetamol in a Pharmaceutical Dose by Adsorptive Voltammetry with a Carbon Paste/La_2O_3 Microcomposite. *Anal. Methods* **2020**, *12*, 2608–2613. [CrossRef]
112. Mangaiyarkarasi, R.; Premlatha, S.; Khan, R.; Pratibha, R.; Umadevi, S. Electrochemical Performance of a New Imidazolium Ionic Liquid Crystal and Carbon Paste Composite Electrode for the Sensitive Detection of Paracetamol. *J. Mol. Liq.* **2020**, *319*, 114255. [CrossRef]
113. Achache, M.; Elouilali Idrissi, G.; Chraka, A.; Ben Seddik, N.; Draoui, K.; Bouchta, D.; Mohamed, C. Detection of Paracetamol by a Montmorillonite-Modified Carbon Paste Sensor: A Study Combining MC Simulation, DFT Computation and Electrochemical Investigations. *Talanta* **2024**, *274*, 126027. [CrossRef] [PubMed]